Journal of Materials Chemistry C

Accepted Manuscript

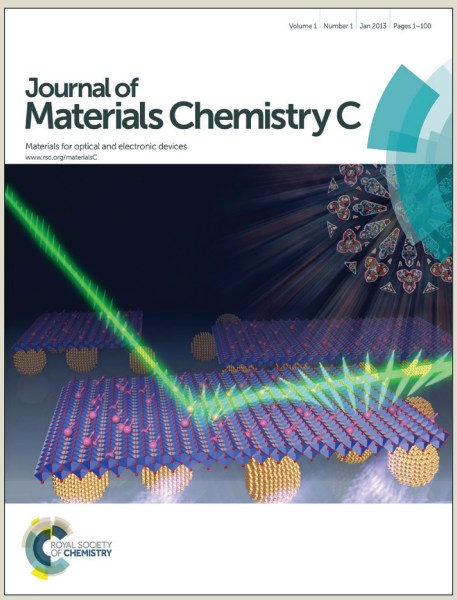

ROYAL SOCIETY OF CHEMISTRY

www.rsc.org/materialsC

Photoluminescent activity of $Ba_{1-x}Ca_xTiO_3$: dependence on particle size and morphology

Agda Eunice Souza[1], Silvio Rainho Teixeira[1], Cássio Morilla-Santos[2], Wido Herwig Schreiner[3], Paulo Noronha Lisboa Filho[4], Elson Longo[5]

[1]Departamento de Física, Química e Biologia, Universidade Estadual Paulista, Faculdade de Ciências e Tecnologia, Presidente Prudente, SP, Brazil

[2]Instituto de Tecnologia para o Desenvolvimento − LACTEC, Universidade Federal do Paraná, Curitiba, PR, Brazil

[3]Departamento de Física, Universidade Federal do Paraná, Curitiba, PR, Brazil

[4]Departamento de Física, Universidade Estadual Paulista, Faculdade de Ciências, Bauru, SP, Brazil.

[5]Instituto de Química, Universidade Estadual Paulista, Araraquara, SP, Brazil

Abstract

It was shown that the higher photoluminescent emission of $Ba_{1-x}Ca_xTiO_3$ titanates is associated with the substitution of Ba by Ca, for the composition x = 0.75, which interferes with structural ordering, morphology and particle growth. Although the XRD data of this sample showed that the crystals do not exhibit long range order, FTIR,

Raman and XPS confirmed the presence of Ti-O bonds in this sample, indicating the particle nucleation of titanates, but without growth and maintaining only short range order. These nanoparticles show perturbations in the symmetry of the unit cell, causing structural distortions, which result in changes in their electronic structure of atoms, destabilizing the whole lattice. This fact gives rise to points of intrinsic defects, changing the intermediate levels in the band gap, subsequently adding to the population of charge carriers and, consequently, radiative recombination with higher photoluminescent emission.

Keywords: titanates, photoluminescence, ordering structure; morphology, particle size.

Introduction

$BaTiO_3$ is a material that has, in addition to ferroelectricity, a high dielectric constant, which make it an attractive material in the field of electro-ceramics and microelectronics, such as capacitors, thermistors with positive temperature coefficients, optical data storage devices of high density, ultrasonic transducers, piezoelectric devices and semiconductors[1-5]. Following the trend of the miniaturization of electronic devices based on electro-ceramic materials, there is great interest in obtaining nanoparticles of semiconductor materials and new conventional ones. The use of ultrafine grains of dielectric materials such as titanates, may help to decrease the thickness of a capacitor and to improve its ability to accumulate charges. Accordingly, interest in the synthesis of nanoscale particles of $BaTiO_3$ has been highlighted in the literature because their electrical properties are largely dependent on grain size and crystal structure[6-7].

$CaTiO_3$ is also part of a class of attractive materials from the point of view of showing some technological properties such as ferroelectricity, electro-mechanical-optical conversion and, in some cases, photoluminescence[5,8]. Due to these properties, $CaTiO_3$ offers a wide technological application and can be used as resistors and dielectric resonators in wireless communication systems[9,10], in immobilizing nuclear waste or as photocatalysts, biomaterials[11] and luminescent (light emitting) devices[5,8,12].

$BaTiO_3$ can form a solid solution with other perovskite ferroelectric materials such as $CaTiO_3$. The partial substitution of Ba in $BaTiO_3$ with Ca results in a piezoelectric property with better stability and may increase electromechanical behavior, increase the stability temperature range for phase transition and inhibit the formation of hexagonal phase $BaTiO_3$[13-15]. Many studies have shown that Ca replaces Ba in $Ba_{1-x}Ca_xTiO_3$ (BCT) to form a tetragonal solid solution up to a solubility limit near 25%, depending on the preparation conditions[13,15,16]. BCT is considered one of the leading candidates for applications such as electro-optic modulator with free charge carriers and memory devices. It is widely used as a ceramic capacitor (including multilayer), and has a better dielectric performance than $BaTiO_3$ not doped or without lattice modifier substitutions[17]. BCTs offer other applications such as filters, antennas, dielectric resonators and doublers, as well as phase shifters and piezoelectric devices. These materials have promising applications in advanced laser systems, optical interconnects, optical storage devices and photorefractive applications, such as phase conjugation or holographic intra-cavity laser mode selection[17].

In this study, barium and calcium titanates ($BaTiO_3$, $CaTiO_3$ and $(BaCa)TiO_3$) were synthesized using the microwave-assisted hydrothermal (MAH) method. BCT phase formation was evaluated for Ba/Ca substitutions at values higher than those found in the literature. Besides, the influence of this substitution on the photoluminescent

properties of these materials was evaluated. A close link was found between photoluminescent properties and structural ordering, particle size and morphological changes in the compounds with Ba/Ca isomorphic substitution.

1. Experimental

$Ba_{1-x}Ca_xTiO_3$ (BCT) was prepared at concentrations of 0, 0.25, 0.50, 0.75, and 1.0 mol. $BaCl_2.2H_2O$, $CaCl_2.2H_2O$ and $C_{12}H_{28}TiO_4$ were used as precursors, and KOH as mineralizer, which acts in the co-precipitation of hydroxides during the initial stage of the synthesis. For each compound, chlorides of the precursors were diluted in a glass Teflon® collector with 20 mL of deionized water. After about 10 minutes, 3.1 mL of titanium tetraisopropanalate were added to the solution, quickly followed by adding 50 mL of KOH (pH 14). During the process, the solution was kept under constant mixing and bubbled nitrogen gas, to minimize the formation of carbonates. Subsequently, the cup with approximately 90% of its total capacity of 110 mL, containing the solution was placed in a reaction cell, hermetically sealed and taken to an adapted home microwave oven for synthesis. The synthesis of these samples was performed at a heating rate of 140°C/min and maintained at 140°C for 40 minutes. During the hold temperature, the maximum pressure recorded was 4 bars. After the reaction time, the system was cooled to room temperature resulting in a clear supernatant and a precipitate of white ceramic powder, which was washed several times with deionized water until the pH of the supernatant was neutral (pH ~ 7). The powder obtained was dried in an oven at 110ºC for 12 hours and characterized by the following methods.

X-ray diffraction was performed using a Shimadzu instrument, model XRD-6000, with Cu $K_{\alpha1}$ (λ = 1.5406 Å) and Cu $K_{\alpha2}$ (λ = 1.5444 Å) radiation, 40 kV, 30 mA. The scan

was done at intervals of 2θ angles from 20° to 120°, using divergence slits of 0.5° and 0.5° reception, with steps of 0.02° and scan rate of 0.2°/min. Raman spectroscopy (Renishaw micro-Raman, inVia model, equipped with a Leica microscope with 50× objective, ~1 μm^2 spatial resolution, and a CCD detector) was performed with spectra scanned between 100 and 1400 cm^{-1} and five accumulations, using a He-Ne laser at a wavelength of 633 nm. Infrared spectroscopy was carried out with a Digilab, model HE Excalibur Series FTS-3100 FTIR instrument in the range of 4000-400 cm^{-1}, in transmittance mode with a resolution of 8 cm^{-1} and 100 scans. UV-visible absorbance (UV-Vis) by diffuse reflectance was performed with a Varian Cary 5G UV-Vis – NIR spectrometer in total reflection mode, using Labsphere reflectance patterns (SRS 94-010 and 02-010 SRD) in the range of 800 to 200 nm at a scan speed of 600 nm/min and lamp replacement (visible-ultraviolet) at 350 nm. Photoluminescence spectroscopy (Thermal Jarrel-Ash Monoscope 27, with a Hamatsu R446 photomultiplier coupled to an acquisition system consisting of a lock-in SR-530) was carried out with excitation energy from a krypton ion laser (Coherent Innova), λ = 350.7 nm and output power of 200 mW. X-ray photoelectron spectroscopy (XPS) (ESCA 3000 Multilab System) was carried out with MgKa radiation, ultra-high vacuum, energy resolution of 0.8 eV and energy calibration considering the Fermi level and the peak of C1s (284.5 eV). Field emission scanning electron microscopy (FE-SEM) was performed with a Zeiss Supra™ model 35 instrument equipped with the detector in the lens for better and higher resolution.

2. Results and Discussion

Figure 1 shows the X-ray diffractograms of the $Ba_{1-x}Ca_xTiO_3$ (BCT) samples. For x = 0, we identified the perovskite barium titanate with a tetragonal structure (**Figure 1 (a)**, JPCDS 83-1878). This tetragonality is discussed in terms of a 2θ peak near 45°. In this case, the peak corresponding to the plane (200) of the cubic phase transforms into a doublet corresponding to the planes (200) and (002) of the tetragonal phase of $BaTiO_3$. The examination of these data is quite complex, because the difference between the lattice parameters (*a* and *b*) of the tetragonal phase is very small and, per hour, can go undetected in X-ray diffraction. However, the results of Raman spectroscopy, which will be discussed later, help to confirm these data. Even for the concentration x = 0, an orthorhombic phase of barium carbonate ($BaCO_3$, JCPDS 1-506) was noted, as shown in **Figure 1 (a)**. The formation of carbonates in the samples may have resulted from atmospheric contamination or, less likely, the presence of the carbon precursor titanium (IV) isopropoxide ($C_{12}H_{28}TiO_4$). After the hydrolysis process, precursor molecules release alcohol (isopropanol), which can undergo secondary reactions due to the heating caused by the hydrothermal microwave and lead to carbonate phases. With the addition of 25% calcium (x = 0.25, **Figure 1 (b)**), the sample also showed the tetragonal phase (JCPDS 81-42) and evidence of a $BaCa(CO_3)_2$ secondary phase (Austonite, JCPDS 3-322). At x = 0.50, the concentration in the diffractogram showed a halo at 2θ near 30° (**Figure 1** insert) indicating that a possible long-range disordered phase could have been present (**Figure 1 (c)**) with the BCT phase (JCPDS 81-42) and a $CaCO_3$ rhombohedral phase (calcite, JCPDS 1-837). When the Ca concentration reached 75% (x = 0.75), the diffraction of this sample showed no BCT phase. The peaks identified corresponded only to calcite already identified in the sample with x = 0.50. However, the halo around 30° became even more pronounced, indicating a compound without a long range order phase coexisting with $CaCO_3$ (**Figure 1 (d)**).

For the sample with x = 1, a single-phase orthorhombic $CaTiO_3$ was identified (**Figure 1 (e)**, JCPDS 82-229).

Figure 1: X-ray diffractograms of $Ba_{1-x}Ca_xTiO_3$ samples: (a) x = 0; (b) x = 0.25; (c) x = 0.50; (d) x = 0.75; (e) x = 1

Figure 2 shows the Raman spectra for the $Ba_{1-x}Ca_xTiO_3$ samples. When x = 0, $BaTiO_3$ has a tetragonal structure with space group *P4mm*. This tetragonality can be confirmed by the vibrational modes identified in Raman spectroscopy (**Figure 2 (a)**). A very strong band around 180 cm^{-1} is attributed to the anharmonic coupling between three A_1(TO) phonons caused by impurities, stress or defects in the network. The position of this band may vary toward slightly higher values of Raman shift, when the particles are a few nanometers in size. The intensity of the band at 305 cm^{-1} is attributed to the overlap of the modes $E(TO_3) + E(LO_2) + B_1^1$, in the 519 cm^{-1} band corresponds to the active transverse modes $E(TO_4) + A_1(TO_3)$[18] and 713 cm^{-1}, the coupling between $E(LO_4)$ and $A_1(LO_3)$ modes resulting in the active mode $E(LO_4) + A_1(LO_3)$[2,19]. The presence of the Raman active mode at 305 cm^{-1} for the B_1 mode indicates an asymmetry of the octahedral [TiO_6] in these samples, characterizing the "fingerprint" of the tetragonal phase of the $BaTiO_3$ sample (x = 0)[18,19]. According to the literature, the band at 305 cm^{-1} along with the band at 713 cm^{-1} of the Raman spectrum gives clear evidence of the tetragonality of nanometric particles of titanates, indicating that there is crystal structure at least locally or tetragonal symmetry at the molecular level[19,20]. These observations could not be directly confirmed by XRD measurements. The band at 1060 cm^{-1} indicates the formation of carbonate ($BaCO_3$) for the sample with x = 0. According

to the work by Baskaran and Chang[21], the Raman spectrum for $BaTiO_3$ samples with partial replacement of Ba by Ca (BCT) does not vary when compared to the spectrum of $BaTiO_3$. There is only a reduction in the bands around 305 cm^{-1} and 713 cm^{-1} with Ca concentration. Moreover, between 182 cm^{-1} and 305 cm^{-1} begin to show small band characteristics of $CaTiO_3$. These bands become pronounced for the sample with x = 1 (**Figure 2 (e)**), where all of the Raman modes are assigned to the orthorhombic perovskite phase according to the literature[9,10,12,22]. According to Hirata and colleagues[23], one hundred seventy-seven vibrational modes are expected for $CaTiO_3$, but many of them cannot be detected due to low polarization. According to Cavalcante and coauthors[22], the orthorhombic structure with space group *Pbnm* with four molecular units in the primitive cell, shows twenty-four Raman active modes represented by $7A_g + 5B_{1g} + 7B_{2g} + 5B_{3g}$. Thus, the nine Raman band modes observed at 177-808 cm^{-1} were assigned to the orthorhombic structure and were consistent with the literature within a narrow range of displacements. According to Cavalcante et al.[22], the positions of the Raman bands may have small displacements depending on the method used in the preparation of the compounds. The bands 177, 224, 244, 285 and 337 cm^{-1} were assigned to bending modes of O–Ti–O. The bands in the region of 224 to 337 cm^{-1} corresponded to the modes associated with rotation of the oxygen chain. The bands at 462 and 537 cm^{-1} characterized the Ti–O torsional mode and at 660 cm^{-1} referred to the symmetric stretching vibration of Ti–O, suggesting distortion of the titanium octahedral[9,10,22]. It was also observed that the sample with x = 1 ($CaTiO_3$) did not display bands characteristic of carbonates, confirming the XRD data. The Raman spectrum of the sample with x = 0.75 did not follow the behavior of previous spectra, as shown in **Figure 2 (d)**. As was emphasized in the discussion of X-ray diffraction, for this concentration, XRD did not identify a long range atomic order for the BCT phase.

However, some peaks corresponding to calcium carbonate ($CaCO_3$) were identified. The Raman spectrum of this sample confirmed the presence of this carbonate by the bands at 280, 1084 and 715 cm^{-1}. In addition to the bands corresponding to vibrational modes of calcium carbonate, there were two Raman bands at 448 and 817 cm^{-1} in the sample. The band at 448 cm^{-1} indicated the torsional vibrational mode of the Ti–O bond, resulting in flexing or internal vibration of the oxygen chain[9,10]. The band at 817 cm^{-1} suggests a vibrational mode that can be related to the order-disorder of cations, usually observed in complex perovskites. The presence of these vibrational modes suggests the formation of a BCT compound with short range order, which may contain the initial formation of clusters or nucleated particles, whose growth should be limited by the degree of the isomorphic substitution modifiers Ba/Ca.

Figure 2: Raman spectra of the $Ba_{1-x}Ca_xTiO_3$ samples: (a) x = 0; (b) x = 0.25; (c) x = 0.50; (d) x = 0.75; (e) x = 1

Figure 3 shows the FTIR spectra of the samples $Ba_{1-x}Ca_xTiO_3$ and **Table 1** show the types associated with the vibrational wavelengths of the absorption bands of the spectra in **Figure 3**. A broadband in the region of 600 cm^{-1} corresponded to the symmetric and asymmetric stretching of the Ti–O octahedron within [TiO_6], featuring its distortion[24]. We observed a broadening and slight shift of this band to higher wavelengths, indicating that the stretch of Ti-O of $BaTiO_3$ (x = 0) leads to the corresponding mode $CaTiO_3$ (x = 1)[23]. According to Jin et al.[25], this shift may be due to the weak Coulomb interactions. These authors believe that during the replacement of cations, some Ca atoms can enter the *B* site of the perovskite ABO_3, although most of

them preferentially occupy the *A* site[25,26]. As the electric charge of the Ca (Ca^{2+}) is lower than that of Ti (Ti^{4+}), the coulomb interaction between the Ca^{2+} and O^{2-} is weaker than that between the Ti^{4+} and O^{2-} (whose bond is preferably covalent), resulting in a decreased energy in the cation-oxygen bond. Thus, the wave number of the absorption band is shifted to higher values with increasing Ca concentration. Another possibility is that when Ca replaces Ba in the BCT network, the cell volume decreases due to the difference in density (or ionic radius) of Ca and Ba. With the decrease in cell volume and with the consequent increase in Coulomb interaction due to the contraction of the Ti–O distance, the wave number of absorption becomes larger[25]. A strong band at around 1460 cm^{-1} is well defined in samples of x = 0.75 and is characteristic of the presence of carbonates, which confirmed the results of XRD and Raman spectroscopy.

According to Ries et al.[27], this band can be interpreted as the C = O vibration, when there are traces of carbonates, a fact that confirms the phases identified by XRD. In the work by Lopez and co-authors[28], the band at 2340 cm^{-1} may indicate CO_2 adsorbed to a metal cation. These authors also suggest that the small band near 1750 cm^{-1} corresponds to an organic carbon which appears in the sample regardless of synthesis route. For x = 1, these parts are not seen, indicating that the C = O vibration is not present, confirming the lack of carbonates for this sample, as observed in the Raman and XRD data. It was also observed for all samples, the presence of a small but sharp band around 1600 cm^{-1}, which is related to the presence of O–H bonds. The bands that appeared around 1350 to 3500 cm^{-1} correspond to the OH^- groups and water of hydration (adsorbed to the particle surface), respectively, common in systems that have hydrogen bonding[14,24]. According to Patil et al.[29], the band at 3500 cm^{-1} may also indicate defects caused by OH^- groups in the titanate lattice.

Figure 3: FTIR spectra of the $Ba_{1-x}Ca_xTiO_3$ samples: (a) x = 0; (b) x = 0.25; (c) x = 0.50; (d) x = 0.75; (e) x = 1

Table 1: Vibration types associated with FTIR wavelengths of the BCT samples

Figure 4 presents the Survey spectra of X-ray photoelectron spectroscopy (XPS) of the $Ba_{1-x}Ca_xTiO_3$ samples. It was possible to identify and quantify in each spectrum the atomic concentrations of photoelectric peaks corresponding to the binding energies of Ba3d, Ca2p, Ti2p, O1s and C1s. It is, naturally, observed a similarity in position of energy peaks C1s, Ti2p and O1s for all samples. For x concentrations varying from 0 to 0.75, the peak corresponding to Ba3d binding energy take also positions analogous, and moreover, with the ion Ca addition in the compound, the peak corresponding to the Ca2p binding energy becomes evident for concentrations $x > 0$. The peaks evidenced for the sample with x = 0.75, clearly show the existence of binding Ba-Ca-Ti-O, confirming some hypotheses raised previously with Raman and FTIR results. According to the XPS results for the sample with x = 0.75, it confirmed the existence of the compound BCT that is certainly found in the initial crystal formation without growth oriented, probably in its original form or in the form of clusters, coexisting with crystalline carbonate particles, a result that had not been previously reported.

Figure 4: XPS spectra of the $Ba_{1-x}Ca_xTiO_3$ samples: (a) x = 0; (b) x = 0.25; (c) x = 0.50; (d) x = 0.75; (e) x = 1

Table 2 presents the theoretical values for the atomic concentrations as well as the experimental values determined by XPS. This technique analyzed the photoelectrons originating from the superficial layers of the samples, which indicates a certain difference from the contents below the surface, especially with respect to calcium. This result associated with the element concentration in the BCT samples explains why the separation of the doublet Ca2p3 and Ca2p1 was observed with absolute clarity only when x = 0.75 (**Figure 4**). With respect to the doublet Ti2p3 and Ti2p1, the same was observed in all samples with the difference in energy around 5.5 eV being observed only for titanium in oxidation state +4.

Table 2: Theoretical percentage and experimental percentage obtained by XPS.

Figure 5 illustrates the deconvolutions performed in the O1s spectrum, adjusted using the Voigt functions (Gauss-Lorentz).

Figure 5: O1s XPS spectra deconvolutions of the $Ba_{1-x}Ca_xTiO_3$ samples: (a) x = 0; (b) x = 0.25; (c) x = 0.50; (d) x = 0.75; (e) x = 1.

The deconvolution curves in the O1s spectra were estimated considering the results obtained in other spectra and literature data. In addition to the Handbook of Photoelectron Spectroscopy X-ray and the website of the National Institute of Standards and Technology, the deconvolutions took into account works from literature [30-34].

In all samples, the contribution related to the hydroxyl (OH^-) found in FTIR measurements, as well as in the literature, and the BCT samples, was considered due to possible humidity and not water molecules within the structure. The deconvolution on barium titanate revealed the presence of barium connected in a segregated phase, in this case in the form of barium carbonate. However, there was no evidence of the presence of carbonates in calcium titanate. The contribution of barium carbonate was also observed in the sample where x = 0.25. The samples where x = 0.75 and 0.50 both showed the presence of calcium carbonate, recalling that the diffraction pattern of the sample where x = 0.75 showed $CaCO_3$ as the major crystalline phase.

The FTIR and XPS data revealed the presence of OH^-, which may have been adsorbed on the material surface and not part of the compound synthesized. However, it has been reported that they act as local defects helping optical properties and favoring some growth mechanisms in certain materials[35,36].

An analysis of **Table 3** shows that the contribution due to the hydroxyl group in the sample is greater when x = 0.75, exceeding the contribution due to metal-oxygen. Moreover, considering the hypotheses with the results of Raman and FTIR, the particles remain in their primitive form, or in the form of clusters, without growth. These nanoparticles have a greater surface area in which a larger number of hydroxyl groups may be adsorbed.

Table 3: Deconvolution contributions in O1s spectrum.

The UV-visible absorption spectra (**Figure 6**) are well defined and have an exponential decay (tail) in the region of lowest energy which indicates the presence of localized states within the band gap, existing even for samples without substitution of cations at the *A* site of $ATiO_3$ of perovskite. According to Longo et al.[37], variations in the values of the optical gap observed for ordered and disordered samples indicate that the exponential optical absorption edge and the optical band gap energy are controlled by the order-disorder structural degree in the titanate lattice. According to the literature, measurements of X-ray absorption (XANES) near the Ti absorption edge show that the order-disorder structural is based on the location of the non-central-symmetrical Ti atom, whose displacement can result in the coexistence of two types of clusters. In one, the Ti atom is surrounded by five oxygen atoms in a pyramidal configuration of square base [TiO_5], and another, octahedral, where the Ti atom is coordinated by six oxygens [TiO_6]. The existence of these two cluster types is evidenced by active modes of Raman spectra, indicating a local symmetry distortion associated with the presence of impurities or oxygen vacancies, very common in perovskites. Similarly, another defect type is possible, in which the cluster is only distorted (tilted) without coordination change. Moreover, the coexistence of [TiO_5]-[TiO_6] clusters and distorted [TiO_6] is the situation most probable to increase the number of intermediate states in the band gap[37-41]. Small variations in the values of the optical gap energy, with increasing concentration of the x cation, as observed in the spectra of **Figure 6**, may be attributed to the way these intermediate states are located within the band gap and the effect of the dimensions of the quantum confinement. The quantum confinement arises when a crystal has nanometric dimensions and has properties intermediate between clusters and bigger crystals (bulk). Contrary to what happens with nanoparticles, variation in the dimensions of a bulk crystal does not significantly influence its properties. With the

partial replacement of Ba/Ca, alterations in the energy gap of these nanoparticles are observed, indicating that the quantum confinement effects participating in the optical behavior of these materials. The optical band gap values were determined by considering the absorption regions of the UV-Vis spectrum, using the Wood and Tauc method[42]. It was observed that the addition of 25% Ca (x = 0.25) in the $BaTiO_3$ network decreased the energy gap by approximately 7%, suggesting changes in the positions of additional levels within the forbidden band. For the sample with x = 0.50, for example, whose spectrum apparently had two absorption regions, the calculation of the energy gap was made considering only the region of higher absorption. Note that in the lower energy region, the exponential tail is less pronounced, showing a higher local distortion. Recall that the XRD spectra of this sample also indicated the presence of a phase without long range order, characterized by a halo around 30°, as discussed above. Thus, the BCT sample with x = 0.50 apparently showed particles with short range order as well as particles with long range order. The sample with x = 0.75 showed an optical gap of approximately 3.8 eV, which was close to that found for the sample with x = 0.50. As described above, although the phase of BCT at x = 0.75 was not identified by XRD data, Raman, FTIR and XPS data clearly showed the presence of this compound. Therefore, it is evident that the value obtained for the optical gap of this sample corresponds to the band gap of the BCT compound and not to the gap energy of carbonates (single phase identified by XRD), which are other optical absorption regions. It appears that the presence of a phase without long range order can strongly influence the formation of intermediate states in the gap. According to the literature, structurally disordered materials exhibit a smooth continuous increase in absorption as a function of energy, and this corroborates the behavior of UV-Vis absorption in this sample. The value of the optical band gap, as well as the absorption curve behavior of the sample

with x = 1 ($CaTiO_3$), is typical of well-ordered crystalline materials and consistent with results in the literature[22,40,43,44]. However, this does not mean that the $CaTiO_3$ structure is free of local defects. There are studies in the literature that show the existence of intermediate states in the band gap of $CaTiO_3$, caused by the displacement of Ti in the lattice to form distorted or complex clusters. Furthermore, theoretical studies have shown that Ca along with Ti makes a strong contribution to the formation of intermediate states near the conduction band (CB)[12,43].

Figure 6: UV-Vis spectra in the absorbance mode × energy of the $Ba_{1-x}Ca_xTiO_3$ samples: (a) x = 0 (b) x = 0.25 (c) = 0.50 x (d) = x 0.75, (e) x = 1 and schematic of additional levels in the band gap derived from the Ti displacement.

Several theoretical studies on the electronic structure of titanates with band mapping results show that the valence band (VB) is derived from the 2p orbitals of oxygen and are separated by a band gap of BC, which derives from the 3d orbital of the Ti transition metal. The top of the oxygen BV is destabilized by the Ti displacement, i.e., by stretching of the Ti–O bond. Therefore, new states are generated located within the band gap of the compound, as can be seen in the illustration inserted at the top of **Figure 6**[37-39,45-48].

Local distortions that generate interband states, behave as an intrinsic defect in this type of perovskite. The UV-Vis absorption region is a useful tool to investigate the degree of local order-disorder of materials, but does not indicate the structural disorder with which the localized states are associated.

Photoluminescent emission (PL) in the visible range depends primarily on the degree of structural disorder, and is connected to the edges of the band structure of the material. It is believed that observed in photoluminescence titanates arises from a radiative recombination between electrons and holes trapped in the states located in the gap. To explain the photoluminescent behavior of titanates, some studies suggest the existence of three types of additional energy levels in the titanate band gap: free exciton levels, STE (self-trapped excitons) levels and defects or impurity levels, all close to the Ti conduction band[49-53]. In general, these authors believe the radiative decay to be a recombination of excited electrons and holes that are coupled in a STE state, which are formed around oxygen vacancies, or a result of free exciton recombination. Oxygen deficiency creates intermediate states in the band gap and the excited electrons recombine with holes through these defect levels[49,50,54,55]. In any event, optical properties such as photoluminescence therefore depend on the structural and electronic properties, including compositional ordering and the presence of impurities and defects. Moreover, PL depends on the electronic excitation and is thus an important complement to spectroscopy of these types of excitations, providing local structural information about the neighborhood of luminescent ions, with a completely different character of information obtained by techniques based on diffraction[41].

Various complex clusters, responsible for the introduction of electronic states within the band gap, act as traps for charge carriers and help to explain the photoluminescence emission. **Figure 7** shows the photoluminescence spectra for the BCT samples. It is observed that the variation in concentration of Ca up to x = 0.50 promoted a proportional increase in the emission process with little displacement in the position of the peak (473 nm at x = 0 to 516 nm at x = 0.50). These results agreed with the UV-Vis absorption results, where reducing the value of the optical band gap

suggests the presence of interband electron levels. The broad band in PL spectra are characteristic of the structural short-range order-disorder shown by these samples and indicates that during radioactive decay, a multiphoton process occurs, i.e., emissions occur by various routes involving numerous states within the prohibited band, originating from intrinsic defects. Longo and co-authors[37], attributed the order to the presence of clusters [TiO_6] and disorder to the increased presence of [TiO_5]. For these authors, the disorder degree may still exist with three different complex clusters: $[TiO_5 \cdot V_O^X]$ state complex, which has two paired electrons and is relatively neutral to the lattice, a $[TiO_5 \cdot V_O^{\bullet}]$ complex state ionized with an unpaired electron, and the $[TiO_5 \cdot V_O^{\bullet\bullet}]$ complex state, which has no unpaired electron and is doubly charged (positive) in relation to the lattice. The partial substitution of Ba by Ca in the $BaTiO_3$ lattice, certainly causes local distortions in the tetragonal network. The literature shows that large ions are energetically favorable to doping with vacancy charge compensation, while smaller ions can self-compensate during replacement, such as Ba/Ca[56] . Okajima et al.[57] studied the effect of this substitution, showing that this exchange occurs easily and that the local structure containing the Ca atom is different from that containing Ba only. Thus, it is likely that the Ca addition contributes to the formation of distorted clusters or broken symmetry for the resulting complex cluster (containing vacancies). The PL is facilitated by the existence of these complex clusters, and these samples show the necessary conditions for emission to occur at room temperature[13,16]. When the Ca concentration was increased to 75% (x = 0.75), there was greater photoluminescence emission and also larger displacement of the central peak to higher wavelengths. As discussed earlier, in this sample, there was a phase without long range order, beyond the $CaCO_3$ crystalline phase. Considering that the calcium carbonate has no significant influence on photoluminescence emission, the highest intensity shown by this sample

could be associated with the existence of different types of cubo-octahedral cluster (containing Ba, Ca or both in partial replacement), coexisting with distorted or complex clusters [TiO_5] and [TiO_6]. The way cubo-octahedral clusters ([BaO_{12}], [CaO_{12}] and/or complexes, oxygen deficient) are associated in the lattice generate a charge distribution very different for each of them, which may significantly contribute to the local disorder and promote intense photoluminescence emission. Orhan and co-authors[48] clearly discuss the existence of pairs of electron-hole carriers (polarons), designated as Jahn-Teller bipolarons, as responsible for radioactive decay. These electron-hole pairs exist before the excitation process, and are considered the main factor that leads to radiative recombination. Moreover, the authors argue that the charge transfer occurs between a [TiO_5] cluster and [TiO_6] cluster, revealing the presence of these intrinsic bipolarons in disordered phases. The excitation energy of 3.52 eV is well below the energy of the optical gap found (3.8 eV) for the sample with x = 0.75. Therefore, it is more evident that there are states within the band gap, or even clusters containing oxygen vacancies, trapping a greater number of charge carriers that undergo recombination. Moreover, as discussed above, there is evidence that the BCT phase exists in its original form at the concentration x = 0.75, without crystal growth or probably still clusters or assembly groups. In other words, the size of the BCT phase crystals is below the X-ray detection limit, and therefore, nanoparticles containing this phase are not identified by X-ray diffraction. Therefore, these particles act as individual point defects (with [TiO_5] and [TiO_6] clusters with oxygen vacancies or simply distorted) promoting the process of radiative recombination in disordered perovskite BCT (x = 0.75). It is known that the presence of nanoparticles less than 100 nm in size are susceptible to quantum effects (polarons trapped in a finite potential well – [TiO_5]-[TiO_6] *clusters*), where properties such as strength, elasticity, conductivity and color can change dramatically and continue

to change, the smaller the size. Therefore, the intense photoluminescence emission of this sample are associated with the particle size of the nanostructured materials, which promote local disorder, increase in the population (polarons) in the intermediate states and facilitate trapping of charge carriers that generate radioactive decay.

Figure 7: Photoluminescence spectra of $Ba_{1-x}Ca_xTiO_3$ samples: (a) x = 0; (b) x = 0.25; (c) x = 0.50; (d) x = 0.75; (e) x = 1

It is also observed in **Figure 7**, that the broadband PL reaches frequencies ranging from violet to red. The photoluminescent contribution in different regions of the visible spectrum is directly related to the different paths traveled by the charge carrier, during exciton recombination (electron-hole pair). Although the material showed a broadband emission photoluminescence spanning nearly the entire visible spectrum, it was possible to evaluate the emission contribution of each compound by analyzing the PL deconvolution of each curve. This procedure has not been reported in the literature for BCT samples with substitution Ba/Ca above 20%. Using Gaussian functions and the software for deconvolution PeakFit, PL curves of all the samples were broken down into four components, each relating to a region of the visible spectrum (**Figure 8**). The contribution of each deconvolution area is shown in the label inserted in each figure. The decomposition band is directly related to the presence of energy levels in the intermediate band gap and each corresponding color represents a different electronic transition which, in turn, is related to a specific structural arrangement, depending on the structural order-disorder degree of the lattice[13]. The origin of the intermediate states within the band gap is due to the broken local symmetry between clusters caused by

distortions, vacancies or interstitial defects, which cause changes in the electronic transition levels. These intermediate states are commonly referred to as shallow and deep defects. Shallow defects are associated with charge carriers trapped near VB or CB clusters, distorted or complex. At these shallow defects are associated more energy photoluminescent emissions, i.e., emissions from violet to yellow occur in electron-hole recombination centers promoted by these defects near the BV and BC[40]. The deep defects are associated with charge carriers trapping farther from VB or CB and are considered the centers responsible for the photoluminescence emission in the lower energy of the visible spectrum (orange and red). The broadband photoluminescence emission is the sum of the individual emissions caused by different shallow and deep defects, which remain concurrently in the material and differ only in the process of recombination between the excitons. It is observed that the addition of Ca to the $BaTiO_3$ lattice to form the compound $Ba_{1-x}Ca_xTiO_3$ causes a change in the contribution of each color (**Figure 8**). For the concentration $x \leq 0.50$, there is decrease in the blue spectral contribution and an increase in the green one. Simultaneously, there is an increase in the relative contribution of the orange band of the spectrum, associated with a small displacement of its peak region to a shorter wavelength. This result shows that the addition of x Ca up to 0.50 in the compound $Ba_{1-x}Ca_xTiO_3$ causes structural changes that contribute to the radiative recombination of charge carriers between regions in deep defects (lower energy), though there is still recombination in the shallow defect region (higher energy). The shift of the orange band contribution of the spectrum to the yellow region, with increase of $x = 0.50$ to $x = 0.75$ Ca concentration, shows that the excitation energy used favors a radiative recombination between charge carriers in the shallow defect region, i.e., to levels near VB and CB. This result is yet more evidence that, although the radioactive decay occurs between the valence bands of oxygen and

conduction band from the titanium, the Ca addition ion lattice modifier is responsible for increasing the local defects, destabilizing energy levels and distorting the clusters of the lattice. These observations show a noticeable difference between the radiative emission process displayed by the pure compounds ($BaTiO_3$ and $CaTiO_3$). While there is a predominance of deep defects in $BaTiO_3$ in $CaTiO_3$, there is a higher concentration of shallow defects, i.e., the polarons generated occupy different positions in the intermediate band gap states of each material. This distinction leads, consequently, to different intensities of radiative emission, as well as the different contributions in each region of visible emission. During the process of electronic excitation (energy scale of 3.52 eV), the compound $BaTiO_3$ can provide non-radiative decay (phonons), because it has a larger amount of intermediate states (suggested by the shape of the UV-Vis curve) to generate one polaron susceptible to radiative recombination. In the case of $CaTiO_3$, the process is similar, but the radiative recombination of polarons is immediate, without the presence of non-radiative decay (or at least less likely), generating a higher photoluminescent intensity than $BaTiO_3$ and photons with higher energy. This fact is evidenced by the presence of shallow defects in this sample, or concentration of electron-hole pairs close to BC and BV.

Figure 8: Photoluminescence deconvolution spectra of the $Ba_{1-x}Ca_xTiO_3$ samples: (a) x = 0; (b) x = 0.25; (c) x = 0.50; (d) x = 0.75; (e) x = 1

It was observed that the partial Ba/Ca replacements caused distortions in the structure of the material and altered its properties. These changes were also visible in the crystal morphology since it is closely related to unit cell growth, the intrinsic

structure of each material. There are several theories to explain crystal growth. Classical growth models assume that the equilibrium morphology of a crystal is defined by minimum surface energy, while non-classical models propose multiple nucleation events for the formation of nanoparticles, which grow an orderly manner to form monocrystalline, polycrystalline or mesocrystaline structures with some degree of orientation[36,58-60]. Meldrum and Cölfen[59] define mesocrystal (*mesoscopically structured crystal*) as the alignment of nanocrystals in a common crystallographic registry, which will shape a particle with any external form, independent of the unit cell geometry. In other words, mesocrystals are superstructures of crystalline nanoparticles, showing rough outer surfaces, and sizes of a few hundred micrometers to the nanometer scale[61]. In general, in a mesoscale transformation, the nanoparticles are interspaced by organic additives but may involve orientational order and self-assembly of faceted microstructures, even in the absence of additives[61]. Accordingly, BCT samples, although containing OH^- groups as additives, identified by FTIR techniques, which can act as binders between the particles and facilitate the self-assembly process that generates mesocrystals. For the $Ba_{1-x}Ca_xTiO_3$ samples, particle morphologies were observed that were from apparently non-classic growth process involving a mechanism of spontaneous self-organization of particles. In this mechanism of self-organization, adjacent particles share a common crystallographic orientation along with a planar interface, resulting in nanoparticles with irregular morphology and typical defects with stacking faults and loss of orientation. Essentially, in this self-organization mechanism, the nanocrystals with common crystallographic orientation aggregate to form a larger crystal[35]. It is at this point that the formation of polycrystalline aggregates, mesocrystals and monocrystalline particles can be observed, which in turn may have originated from

an intermediate mesocrystal in non-classical growth. These transformations are highlighted in **Figure 9**.

Figure 9: FE-SEM images of $Ba_{1-x}Ca_xTiO_3$ samples (x = 0.50): Particles looking like mesocrystals

Figure 10 shows FE-SEM images of the $Ba_{1-x}Ca_xTiO_3$ samples. For x = 0 (**Figure 10a**), polycrystalline agglomerates of $BaTiO_3$ nanoparticles are seen. They appear predominantly rounded, and though they do not have faceted surfaces, an increase in agglomeration can be observed. It is observed that the addition of Ca modifies the microstructure of the particles leading to a cubic morphology at intermediate concentrations. Note that with x = 0.25 (**Figure 10b**) rounded particles appear, showing the start of a faceting process, but without much defined geometry. At the concentration x = 0.50 (**Figure 10c**), the samples show large agglomerates of cubic particles and some small cubes with edge defined and defective surface, again showing apparent mesocrystal formation and larger polycrystalline particles. This is an important aspect in the formation of mesocrystals through the self-assembly process, which are spontaneously occurring events leading to structure formation. In other words, smaller particles are joined in a predefined interaction that results in an ordered and spontaneous final specific form[36]. On the other hand, it is also known that grain growth occurs by diffusion during the sintering process and requires high temperatures. As the samples were maintained at a relatively low temperature (140°C), it is possible overheating occurred during the specific synthesis process, generating hot spots that promote diffusion phenomena with coalescence and grain growth[62]. The addition of 75% Ca to

the $BaTiO_3$ lattice (x = 0.75, **Figure 9d**), results in a morphology less defined than the previous one, and a reduction in the size of the nanoparticles. Numerous agglomerates of cubic nanoparticles are observed, which join forming apparently other small cubes or spherical agglomerates, clearly showing grain boundaries between them (see magnification in **Figure 11**). Anyway, these particles can also represent the formation of mesocrystals from the organization of nanosized particles. Cölfen and Antonietti[61] defined the mesocrystals as a particular case of colloidal crystals. According to these authors, the colloidal particles result from a formal substitution of atoms or molecules in a classical crystallization event and are defined by monodisperse nanoparticles, which leads to a super-lattice with new and desirable properties, such as a photonic band gap or altered optical and electronic properties, as in the case of semiconductors[61]. The concepts presented by these authors help explain the intense photoluminescence emission, the growth and particle morphology of the BCT samples. However, it is believed that the nanoparticles constituting the small agglomerates or mesocrystals have a large amount of local defects, generated by the presence of distorted clusters in conjunction with the cluster complexes containing a Ti atom. These clusters can act as individual and independent nucleation centers, which consequently assist in high photoluminescence. With x = 1 (**Figure 10e**), $CaTiO_3$ particles exhibit some variation in morphology. In these images, there are small agglomerates with apparently spherical morphologies together with cubic agglomerates, again indicating self-organized growth. The images show that cubic morphology is characterized by the presence of the lattice modifier (Ca) in the structure of the $Ba_{1-x}Ca_xTiO_3$ compound. The loss of the characteristic cubic architecture at x = 0.75 concentration, is related to the extrapolation limit of accommodations of the Ca ion in the lattice of the compound, which causes a series of defects, preventing this structure from being repeated over long atomic

distances and thereby inhibiting crystal growth to form particles of defined morphology and higher dimensions. In other words, the morphology of undefined geometry is, therefore, associated with the nucleation of BCT particles, with no growth, which is associated with the generation of defects. These peculiar features give a false interpretation of "*amorphous phase*", suggested by the XRD data, which is associated with intense photoluminescence emission reported by most studies in the literature. However, as found in this work, the "*amorphous phase*" that generates intense photoluminescence emission of the compound $Ba_{1-x}Ca_xTiO_3$ (x = 0.75) is only nucleated nanoparticles without growth and, consequently, without apparent geometry and dispersed in the material.

Figure 10: FE-SEM images of $Ba_{1-x}Ca_xTiO_3$ samples: (a) x = 0, (b) x = 0.25, (c) x = 0.50, (d) x = 0.75, (e) x = 1

Figure 11: FE-SEM images of $Ba_{1-x}Ca_xTiO_3$ samples (x = 0.75) magnification.

It is evident that the $Ba_{1-x}Ca_xTiO_3$ compound has intrinsic behavior, as to the structural formation, morphology and photoluminescent properties. The optical property is strongly dependent on the structural and morphological characteristics of the crystalline system of each compound. Among these factors, the order-disorder effects, associated with the particle size, the surface state, and lattice defects are considered crucial factors in the photoluminescence interpretation of the material. This combination of factors associated with the results presented in this paper explain the anomalous behavior of the $Ba_{1-x}Ca_xTiO_3$ sample with the concentration x = 0.75. This sample does not exhibit long range order, although showing evidence of nucleation phase BCT

without growth, which characterizes a blurring morphology and extremely small particles in the FE-SEM images. Their photoluminescent properties are considerably outstanding compared to other concentrations of Ca in the lattice. Partial substitution of the lattice modifier Ca acts directly on the structural formation of the compound, causing intrinsic defects during the formation of clusters. These defects, in turn, are maximized at x = 0.75, concentration, i.e., the band gap intermediate levels are increased, along with the population of charge carriers for radiative recombination during the excitation process. Simultaneously, the oriented growth of particles is inhibited, at the threshold of BCT phase formation, thereby leaving nucleated particles which act as individual centers of defects, which reciprocally promote the intense photoluminescence emission of this sample. This whole process is illustrated in **Figure 12**.

Figure 12: Schematic illustration of the defects caused by the partial substitution of lattice modifier in the compound $Ba_{1-x}Ca_xTiO_3$

3. Conclusions

Studies revealed that $Ba_{1-x}Ca_xTiO_3$ (BCT) compounds with perovskite-type structure are formed, in addition to the solubility limit of Ca in the $BaTiO_3$ lattice described in the literature. Although not identified in the XRD spectra, it was found that at the concentration x = 0.75, the BCT phase forms without ordered structure at long atomic distances. This result suggests that the BCT compound particles are nucleated and do not grow oriented with a definitive morphology, behaving as individual centers of defects. In this case the nanoparticles formed have dimensions that give to quantum

confinement an important contribution to the optical behavior of this material. Moreover, the largest volume of smaller particles has a higher surface area, ie a higher concentration of defects. These features promote the high photoluminescence emission exhibited by this material, suggesting a potential candidate for optical applications.

Acknowledgements

This work is supported by FAPESP/CEPID, CNPq and INCTMN. The authors thank Prof. Dr Maximo Li Siu, of the Physical Institute of USP-São Carlos, and Rorivaldo Camargo of the LIEC-São Carlos for scientific and technical support.

References

1 W-S Cho, Structural evolution and characterization of $BaTiO_3$ nanoparticles synthesized from polymeric precursor. *J. Phys. Chem. Solids*, 1998, **59**, 659-666.

2 Y. Shiratori, C. Pithan, J. Dorseiffer, R. Waser, Raman scattering studies on nanocrystalline $BaTiO_3$ Part I – isolated particles and aggregates. *J. Raman Spectroscopy*, 2007, **38**, 1288-1299.

3 Y. Shiratori, C. Pithan, J. Dorseiffer, R. Waser, Raman scattering studies on nanocrystalline $BaTiO_3$ Part II – consolidated polycrystalline ceramics. *J. Raman Spectroscopy*, 2007, **38**, 1300-1306.

4 S. Sreekantan, A. F. M. Noor, Z. A. Ahmad, R. Othman, A. West, Structural and electrical characteristic of crystalline barium titanate synthesized by low temperature aqueous method. *J. Mater. Process. Tech.* 2008, **195**, 171-177.

5 W. Dong, B. Li, X. Wang, L. An, C. Li, B. Chen, G. Wang, Z. Shi, General Approach to well-defined perovskite $MTiO_3$ (M = Ba, Sr, Ca, and Mg) nanostructures. *J. Phys. Chem. C*, 2011, **115**, 3918-3925.

6 X. Zhu, J. Wang, Z. Zhang, J. Zhu, S. Zhou, Z. Liu, N. Ming, Perovskite nanoparticles and nanowires: Microwave-hydrothermal synthesis and structural characterization by high-resolution transmission electron microscopy. *J. Am. Ceram. Soc*., 2008, **91**, 2683-2689.

7 D. Sarkar, Syntesis and Properties of $BaTiO_3$ Nanopowders. *J. Am. Ceram. Soc*., 2011, **94**, 213-217.

8 S. Lazaro, J. Milanez, A. T. Figueiredo, V. Longo, V. R. Mastelaro, F. S. Vicente, A. C. Hernandes, J. A. Varela, E. Longo, Relation between photoluminescence emission and local order-disorder in $CaTiO_3$ lattice modifier. *Appl. Phys. Lett.*, 2007, **90**, 111904-1-3.

9 H. Zheng, H. Bagshaw, G. D. C. C. Györgyfalva, I. M. Reaney, R. Ubic, J. Yerwood, Raman spectroscopy and microwave properties of $CaTiO_3$-based ceramics. *J. Appl. Phys*., 2003, **94**, 2948-2956.

10 H. Zheng, H. Bagshaw, G. D. C. C. Györgyfalva, I. M. Reaney, R. Ubic, J. Yerwood, Raman spectroscopy B-site order-disorder in $CaTiO_3$ –based microwave ceramics. *J. Eur. Cer. Soc.*, 2003, **23**, 2653-2659.

11 A. P. Rodrigues, M. Inoue, T. Tanaka, M. Miyake, A. M. Sfer, E. Kishimoto, H. Tsujigiwa, R. S. Rivera, H. Nagatsuka, Effect of $CaTiO_3$–$CaCO_3$ prepared by alkoxide method on cell response. *J. Bio. Mater. Res. Part A*, 2009, **93**, 297-303.

12 V. S. Marques, L. S. Cavalcante, J. C. Sczancoski, D. P. Volanti, J. W. M. Espinosa, M. R. Joya, M. R. M. C. Santos, P. S. Pizani, J. A. Varela, E. Longo, Influence of microwave energy on structural and photoluminescent behavior of $CaTiO_3$ powders. *Solid State Sci.*, 2008, **10**, 1056-1061.

13 F. V. Motta, A. T. Figueiredo, V. M. Longo, V. R. Mastelaro, A. Z. Freitas, L. Gomes, N. D. Vieira, E. Longo, J. A. Varela, Disorder-dependent photoluminescence in $Ba_{0.8}Ca_{0.2}TiO_3$ at room temperature. *J. Lumin*., 2009, **129**, 686-690.

14 A. K. Rai, K. N. Rao, L. V. Kumar, K. D. Mandal, Synthesis and characterization of ultra fine barium calcium titanate, barium strontium titanate and $Ba_{1-2x}Ca_xSr_xTiO_3$ (x = 0.05-0.10). *J. Alloys Comp.*, 2009, **475**, 316-320.

15 Q. Yang, L. Fang, F. Zheng, M. Shen, Structural, electrical, luminescent, and magnetic properties of $Ba_{0.77}Ca_{0.23}TiO_3$:Eu ceramics. *Mater. Chem. Phys*., 2009, **118**, 484-489.

16 F. V. Motta, A. P. A. Marques, J. W. M. Espinosa, P. S. Pizani, E. Longo, J. A. Varela, Room temperature photoluminescence of BCT prepared by complex polimeric method. *Curr. Appl. Phys*., 2010, **10**,16-20.

17 M. R. Panigrahi, S. Panigrahi, Structural analysis of 100% relative intense peak of $Ba_{1-x}Ca_xTiO_3$ ceramics by X-ray powder diffraction method. *Phys. B*, 2010, **405**, 1787-1791.

18 M. L. Moreira, G. P. Mambrini, D. P. Volanti, E. R. Leite, M. O. Orlandi, P. S. Pizani, V. R. Mastelaro, C. O. Paiva-Santos, E. Longo, J. A. Varela, Hydrothermal Microwave: a new route to obtain photoluminescent crystalline $BaTiO_3$ nanoparticles. *Chem. Mater.*, 2008, **20**, 5381-5387.

19 M-W. Chu, Y. Shingaya, T. Nakayama, Effect of 90° ferroelastic twin walls on lattice dynamics of nanocrystalline tetragonal ferroelectric perovskites. *Appl. Phys. A*, 2007, **86**, 101-106.

20 G. Yang, Z. Yue, T. Sun, J. Zhao, Z. Yang, L. Li, Investigation of ferroelectric phase transition for modified barium titanate in multilayer ceramic capacitors by situ Raman scattering and dielectric measurement. *Appl. Phys. A*, 2008, **91**, 119-125.

21 N. Baskaran, H. Chang, Thermo-Raman and dielectric constant studies of $Ca_xBa_{1-x}TiO_3$ ceramics. *Mater. Chem. Phys*., 2002, **77**, 889-894.

22 L. S. Cavalcante, V. S. Marques, J. C. Sczancoski, M. T. Escote, M. R. Joya, J. A. Varela, M. R. M. C. Santos, P. S. Pizani, E. Longo, Syntesis, structural refinement and optical behavior of $CaTiO_3$ powders: A comparative study of processing in different furnaces. *Chem. Eng.*, 2008, **143**, 299-307.

23 T. Hirata, K. Ishioka, M. Kitajuma, Vibrational spectroscopy and X-ray diffraction of perovskite compounds $Sr_{1-x}M_xTiO_3$ (M = Ca, Mg; $0 \leq x \leq 1$). *J.Solid State Chem.*, 1996, **124**, 353-359.

24 L. Wang, H. Kang, D. Xue, C. Liu, Synthesis and characterization of $Ba_{0,5}Sr_{0,5}TiO_3$ nanoparticles. *J. Crys.Growth*, 2009, **311**, 605-607.

25 X. Jin, D. Sun, Y. Zhang, J. Qian, Investigation on FTIR spectra of barium calcium titanate ceramics. *J. Electrocer.*, 2009, **22**, 285-290.

26 J-S. Park, Y-H. Lee, K-B. Kim, Y-I Kim, Structural study of Ca doped barium titanate. *Nuclear Instruments and Methods in Physics Research B*, 2012, **284**, 44-48.

27 A. Ries, A. Z. Simoes, M. Cilense, M. A. Zaghete, J. A. Varela, Barium strontium titanate powder obtained by polymeric precursor method. *Mater. Charac.*, 2003, **50**, 217-221.

28 M. C. B. López, G. Fourlaris, B. Rand, F. L. Riley, Characterization of barium titanate powders: barium carbonate identification. *J. Am. Cer. Soc.*, 1999, **82**, 1777-1786.

29 S. K. Patil, N. Shah, F. D. Blum, M. N. Kahaman, Fourier transform infrared analysis of hydroxyl content of hydrothermally processed heteroepitaxial barium titanate films. *J. Mater. Res.*, 2005, **20**, 3312-3319.

30 C. Miot, E. Husson, C. Proust, R. Erre, J. P. Coutures, X-ray photoelectron spectroscopy characterization of barium titanate ceramic prepared by the citric route. Residual carbon study. *J. Mat. Res*., 1997, **12**, 2388-2392.

31 R. Ayouchi, F. Martín, J. R. Ramos-Barrado, D. Leinen, Compositional, structural and electrical characterization of barium titanate thim films prepare don fused silica and Si(111) by spray pyrolysis. *Surf. Interface Anal.*, 2000, **30**, 565-569.

32 N. Ohtsu, K. Sato, K. Saito, K. Asami, T. Hanawa, Calcium phosphates formation on $CaTiO_3$ coated titanium. *J. Mater. Sci.: Mater. Med.*, 2007, **18**, 1009-1016.

33 K-i. Minura, K. Hiramatsu, M. Mariya, W. Sakamoto, S. Kawado, Y. Uesu, Y. Yogo, Opitical properties of transparent barium titanate nanoparticle/polymer hybrid synthesized from metal alkoxides. *J. Nanopart. Res.*, 2010, **12**, 1993-1943.

34 C-Y. Chen, K. Ozasa, K-i. Katsumata, M. Maeda, K. Okada, N. Matsushita, $CaTiO_3$ nanobricks prepared from anodized TiO_2 nanotubes. *Electrochemistry Communications*, 2012, **22**, 101-104.

35 M. L. Moreira, J. Andrès, V. R. Mastelaro, J. A. Varela, E. Longo, On the reverse crystal growth of $BaZrO_3$ decaoctahedron: shape evolution and mechanism. *CrysEngComm*, 2011, **13**, 5818-5824.

36 H. Cölfen, M. Antonietti, *Mesocrystals and Nonclassical Crystallization*, USA, John Wiley & Sons, Ltd., 2008.

37 V. M. Longo, A. T. Figueiredo, A. Lázaro, M. F. Gurgel, M. G. S. Costa, C. O. Paiva-Santos, J. A. Varela, E. Longo, V. R. Mastelaro, F. S. Vicente, A. C. Hernandes, R. W. A. Franco, Structural conditions that leads to photoluminescnce emission in $SrTiO_3$: an experimental and theoretical approach. *J. Appl. Phys.*, 2008, **104**, 023515-1-11.

38 E. Orhan, F. M. Pontes, C. D. Pinheiro, T. M. Boschi, E. R. Leite, P. S. Pizani, A. Beltrán, J. Andrés, J. A. Varela, E. Longo, Origin of photoluminescence in $SrTiO_3$: a combined experimental and theorical study. *J.Solid State Chem*., 2004, **177**, 3879-3885.

39 V. M. Longo, L. S. Cavalcante, M. G. S. Costa, M. L. Moreira, A. T. Figueiredo, J. Andrés, J. A. Varela, E. Longo, First principles calculations on the origin of violet-blue and Green light photoluminescence emission in SrZrO3 and SrTiO3 perovskites. *Theor. Chem. Acc.*, 2009, **124**, 385-394.

40 M. L. Moreira, E. C. Paris, G. S. Nascimento, V. M. Longo, J. R. Sambrano, V. R. Mastelaro, M. I. B. Bernardi, J. Andrés, J. A. Varela, E. Longo, Structural and optical properties of $CaTiO_3$ perovskite-based materials obtained by microwave-assisted hydrothermal synthesis: Na experimental and theorical insight. *Acta Materialia*, 2009, **57**, 5174-5185.

41 V. M. Longo, M. G. S. Costa, A. Z. Simões, I. L. V. Rosa, C. O. Paiva-Santos, J. Andrés, E. Longo, J. A. Varela, On the photoluminescence behavior of samarium-doped strontium titanate nanostructure under UV light. A structural and electronic understanding. *Phys. Chem. Chem. Phys*., 2010, **12**, 7566-7579.

42 D. L. Wood, J. Tauc, Weak absorption tails in amorphous semiconductors. *Phys. Rev. B*, 1972, **5**, 3144-3151.

43 F. M. Pontes, C. D. Pinheiro, E. Longo, E. R. Leite, S. R. Lazaro, J. A. Varela, P. S. Pizani, T. M. Boschi, F. Lanciotti, The role of network modifiers in the creation of photoluminescence in $CaTiO_3$. *Mater. Chem. Phys.*, 2002, **78**, 227-233.

44 J. Milanez, A. T. Figueiredo, S. Lazaro, V. M. Longo, R. Erlo, V. R; Mastelaro, R. W. A. Franco, E. Longo, J. A. Varela, The role of oxygen vacancy in the photoluminescence property at room temperature of the $CaTiO_3$. *J. Appl. Phys*., 2009, **106**, 0435261-04352617.

45 C. D. Pinheiro, E. Longo, E. R. Leite, F. M. Pontes, R. Magnani, J. A. Varela, P. S. Pizani, T. M. Boschi, F. Lanciotti, The role of defect state in the creation of photoluminescence in $SrTiO_3$. *Appl. Phys. A*, 2003, **77**, 81-85.

46 E. Longo, E. Orhan, F. M. Pontes, C. D. Pinheiro, E. R. Leite, J. A. Varela, P. S. Pizani, T. M. Boschi, Jr, F. Lanciotti, A. Beltrán, J. Andrés, Density functional theory calculation of the electronic structure of $Ba_{0.5}Sr_{0.5}TiO_3$: Photoluminescent properties and structural disorder. *Phys. Rev. B*, 2004, **69**, 125115-1-7.

47 C. B. Samantaray, H. Sim, H. Hwang, Electronic structure and optical properties of barium strontium titanate ($Ba_xSr_{1-x}TiO_3$) using first-principles methods. *Phys. B*, 2004, **351**, 158-162.

48 E. Orhan, J. A. Varela, A. Zenatti, M. F. C. Gurgel, F. M. Pontes, E. R. Leite, E. Longo, P. S. Pizani, A. Beltràn, J. Andrès. Room-temperature

photoluminescence of $BaTiO_3$: Joint experimental and theoretical study. *Phys. Rev. B*, 2005, **71**, 085113-1-7.

49 W. F. Zhang, Z. Yin, M. S. Zhang, Z. L. Du, W. C. Chen, Roles of defects and grain sizes in photoluminescence of $SrTiO_3$. *J. Phys. Cond. Mater.*, 1999, **11**, 5655-5660.

50 D. Kan, T. Terashima, R. Kanda, A. Masuno, K. Tanaka, S. Chu, H. Kan, A. Ishizumi, Y. Kanemitsu, Y. Shimakawa, Takano, M. Blue-light emission at room temperature from Ar^+-irradieted $SrTiO_3$. *Nature Mater. Lett.*, 2005, **4**, 816-819.

51 C. B. Samantaray, H. Sim, H. Hwang, First-principle study of electronic structure and optical properties of barium strontium titanate ($Ba_xSr_{1-x}TiO_3$). *Appl. Surf. Sci.*, 2005, **250**,146-151.

52 Y. Kanemitsu, Y. Yamada, Light emission from $SrTiO_3$. *Phys. Status Solidi B*, 2011, **248**, 416-421.

53 Y. Yamada, Y. Kanemitsu, Blue Light emission from strongly photoexcited and electron-doped $SrTiO_3$. *J. Appl. Phys.*, 2011, **109**, 1024101-1024104.

54 W. Zhang, H. Wang, J. Chen, W. Zhang, X. Xiong, J. Zhang, Photoluminescence at room temperature in polycrystalline $Ba_xSr_{1-x}TiO_3$ ceramics obtained by solid-state reaction method. *J. Lumin.*, 2008, **128**, 1359-1362.

55 A. Rubano, D. Paparo, F. M. Granozio, S. Di Uccio, L. Marrucci, Blue luminescence of $SrTiO_3$ under intense optical excitation. *J. Appl. Phys.*, 2009, **106**, 1035151-10351511.

56 J. A. Dawson, X. Li, C. L. Freeman, J. H. Harding, D. C. Sinclair, The application of a new potential model to the rare-earth doping of $SrTiO_3$ and CaTiO3. *J. Mater. Chem. C*, 2013, **1**, 1574-1582.

57 T. Okajima, K. Yasukawa, N. Umesaki, Local structure of Ca dopant in $BaTiO_3$ by K-edge X-ray absorption near-edge structure and first-principle calculations. *J. Elec. Spect. Rel. Phen.*, 2010, **180**, 53-57.

58 Y. M. Chiang, D. III Birnie, W. D. Kingery, *Physical ceramics: Principles for ceramic science and engeneering.* New York, *John Wiley & Sons*, cap. 1, p. 1-95, 1997.

59 F. C. Meldrum, H. Cölfen, Controlling mineral morphologies and structures in biological and synthetic systems. *Chem. Rev.*, 2008, **108**, 4332-4432.

60 A. N. Kulak, P. Iddon, Y. Li, S. P. Armes, H. Cölfen, O. Paris, R. M. Wilson, F. C. Meldrum, Continuous structural evolution of calcium carbonate

particles: a unifying model of copolymer-mediated crystallization. *J. Am. Chem. Soc.*, 2007, **129**, 3729-3736.

61 H. Cölfen, M. Antonietti, Mesocrystals: inorganic superstructure made by highly parallel crystallization and controlled alignment. *Ang. Chemie Inter. Ed.*, 2005, **44**, 5576-5591.

62 R. R. Menezes, P. M. Souto, R. H. G. A. Kiminami, Sinterização de cerâmicas em microondas. Parte I: Aspectos fundamentais *Cerâmica*, 2007, **53**, 1-10.

Graphical table of contents

Photoluminescent Activity of $Ba_{1-x}Ca_xTiO_3$: dependence on particle size and morphology

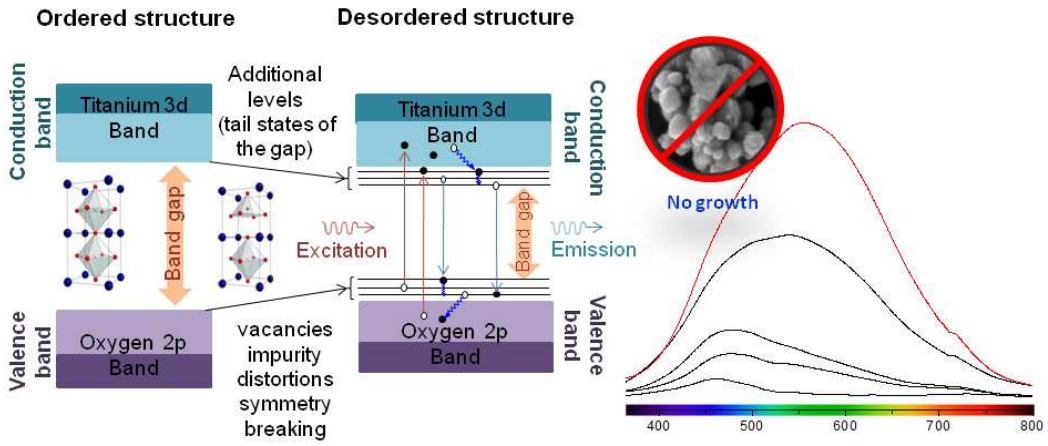

Substitution of Ba/Ca (0.25/0.75) in $Ba_{1-x}Ca_xTiO_3$ compounds cause defects which inhibit the growth of particles and promote a higher photoluminescent emission.

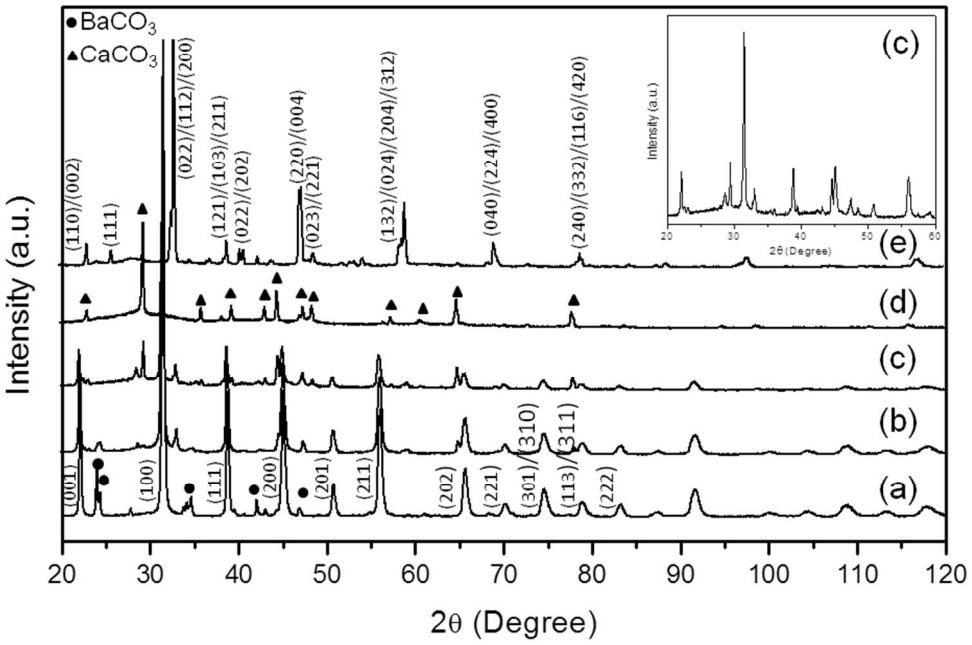

Figure 1: X-ray diffractograms of Ba1-xCaxTiO3 samples: (a) x = 0; (b) x = 0.25; (c) x = 0.50; (d) x = 0.75; (e) x = 1
254x190mm (96 x 96 DPI)

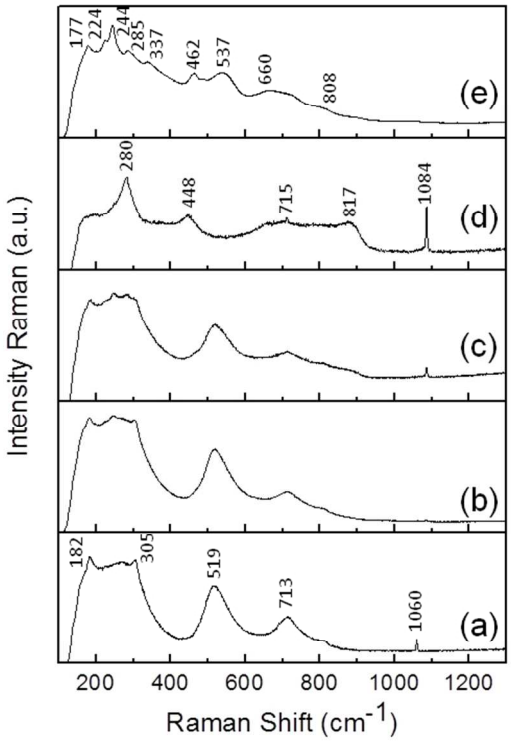

Figure 2: Raman spectra of the Ba1-xCaxTiO3 samples: (a) x = 0; (b) x = 0.25; (c) x = 0.50; (d) x = 0.75; (e) x = 1
254x190mm (96 x 96 DPI)

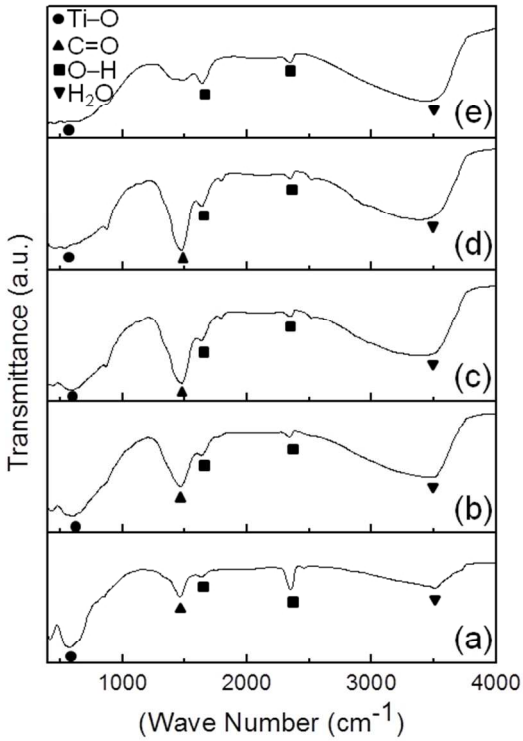

Figure 3: FTIR spectra of the Ba1-xCaxTiO3 samples: (a) x = 0; (b) x = 0.25; (c) x = 0.50; (d) x = 0.75; (e) x = 1
254x190mm (96 x 96 DPI)

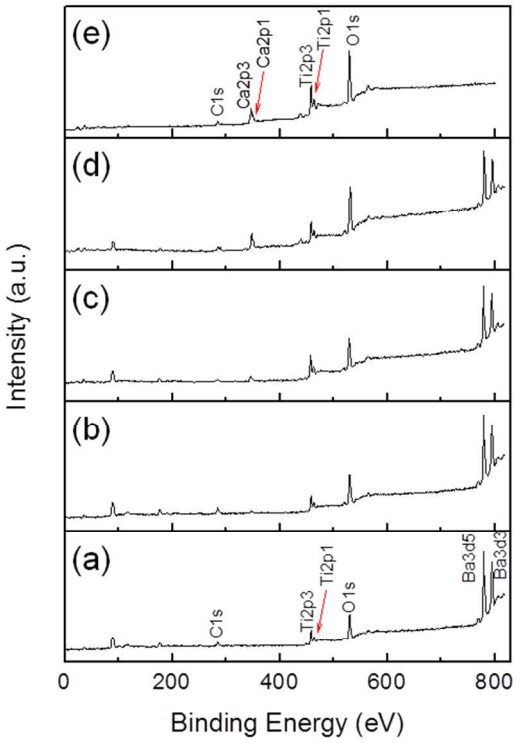

Figure 4: XPS spectra of the Ba1-xCaxTiO3 samples: (a) x = 0; (b) x = 0.25; (c) x = 0.50; (d) x = 0.75; (e) x = 1
254x190mm (96 x 96 DPI)

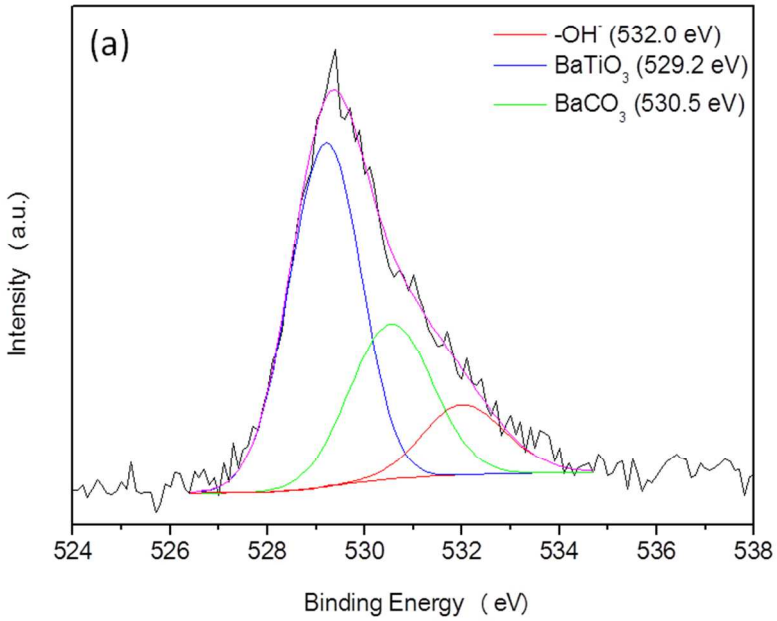

Figure 5: O1s XPS spectra deconvolutions of the Ba1-xCaxTiO3 samples: (a) x = 0; (b) x = 0.25; (c) x = 0.50; (d) x = 0.75; (e) x = 1
254x190mm (96 x 96 DPI)

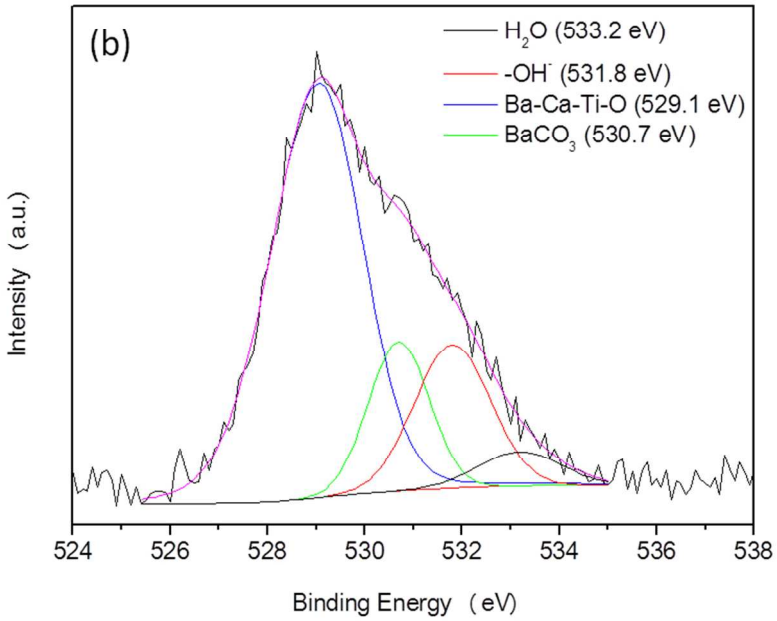

Figure 5: O1s XPS spectra deconvolutions of the Ba1-xCaxTiO3 samples: (a) x = 0; (b) x = 0.25; (c) x = 0.50; (d) x = 0.75; (e) x = 1
254x190mm (96 x 96 DPI)

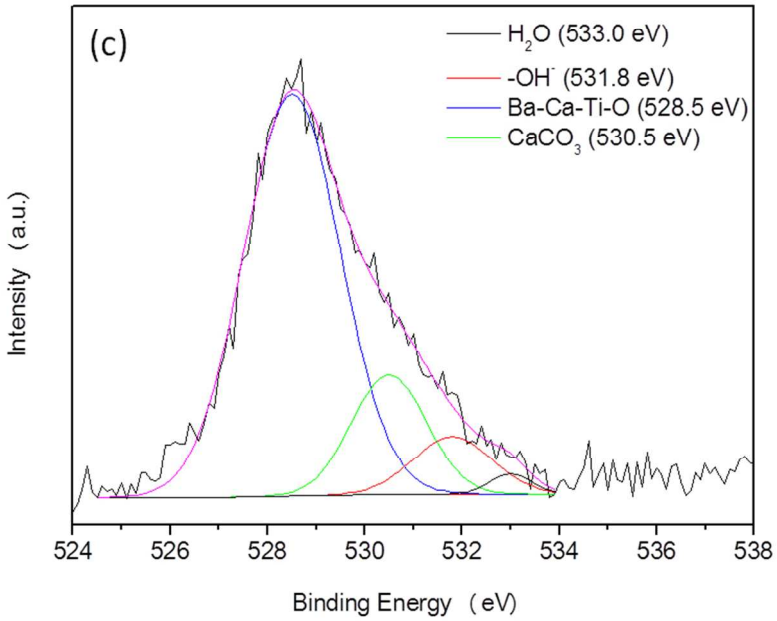

Figure 5: O1s XPS spectra deconvolutions of the Ba1-xCaxTiO3 samples: (a) x = 0; (b) x = 0.25; (c) x = 0.50; (d) x = 0.75; (e) x = 1
254x190mm (96 x 96 DPI)

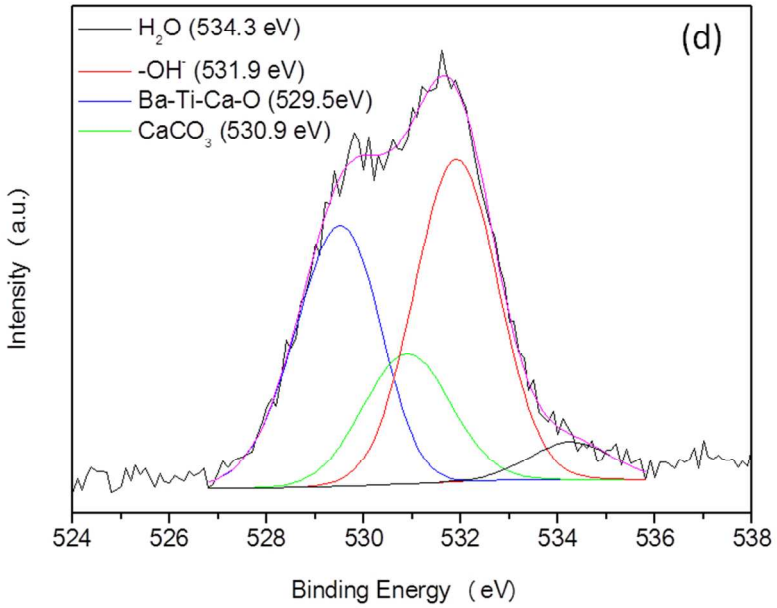

Figure 5: O1s XPS spectra deconvolutions of the Ba1-xCaxTiO3 samples: (a) x = 0; (b) x = 0.25; (c) x = 0.50; (d) x = 0.75; (e) x = 1
254x190mm (96 x 96 DPI)

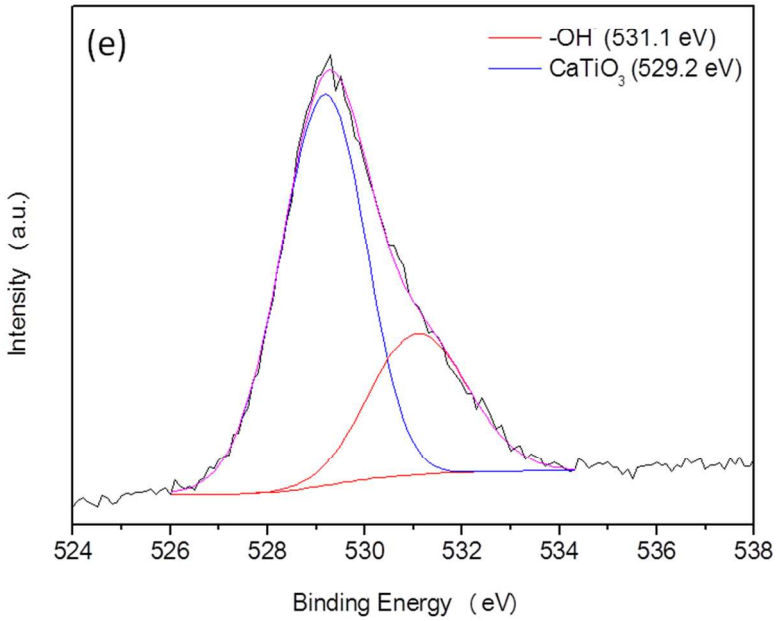

Figure 5: O1s XPS spectra deconvolutions of the Ba1-xCaxTiO3 samples: (a) x = 0; (b) x = 0.25; (c) x = 0.50; (d) x = 0.75; (e) x = 1
254x190mm (96 x 96 DPI)

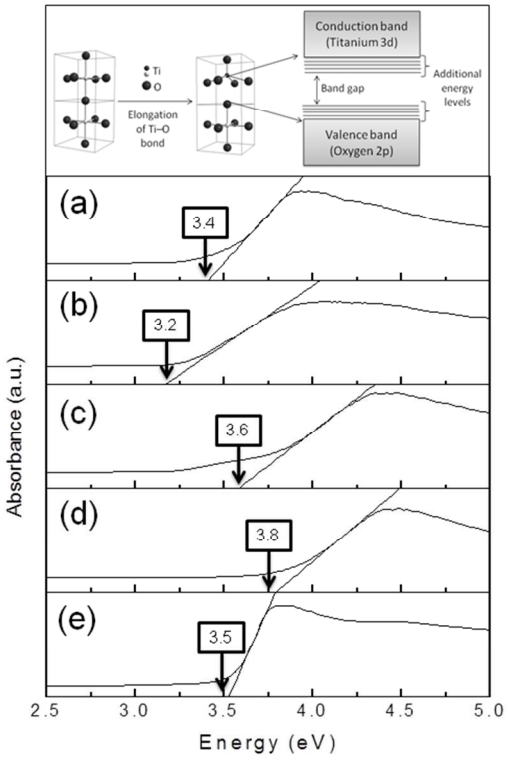

Figure 6: UV-Vis spectra in the absorbance mode × energy of the Ba1-xCaxTiO3 samples: (a) x = 0 (b) x = 0.25 (c) = 0.50 x (d) = x 0.75, (e) x = 1 and schematic of additional levels in the band gap derived from the Ti displacement
254x190mm (96 x 96 DPI)

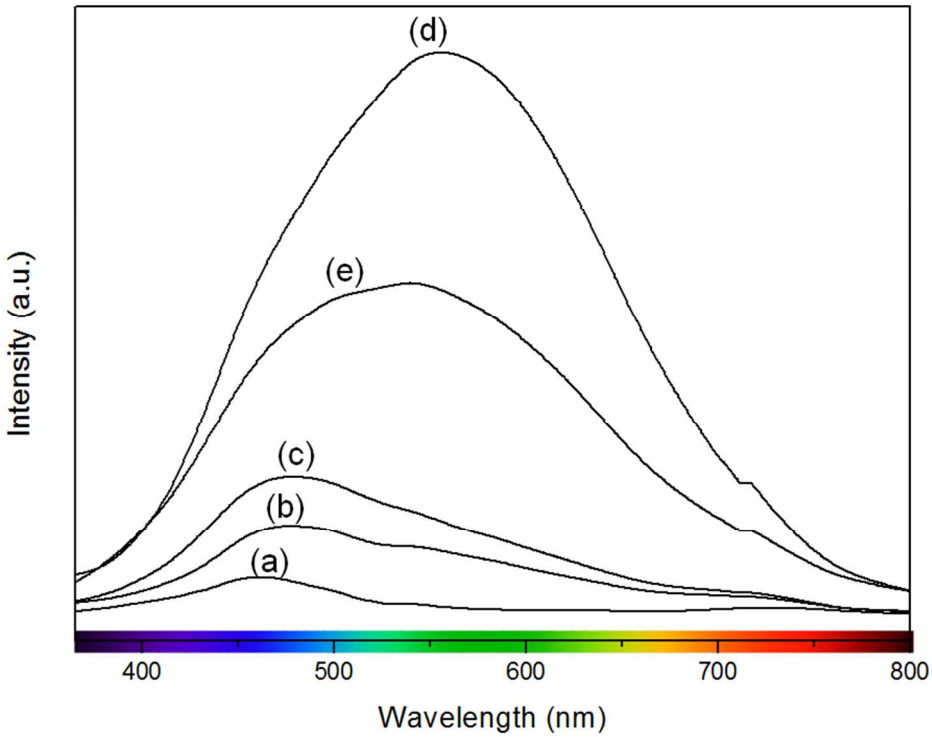

Figure 7: Photoluminescence spectra of Ba1-xCaxTiO3 samples: (a) x = 0; (b) x = 0.25; (c) x = 0.50; (d) x = 0.75; (e) x = 1
254x190mm (96 x 96 DPI)

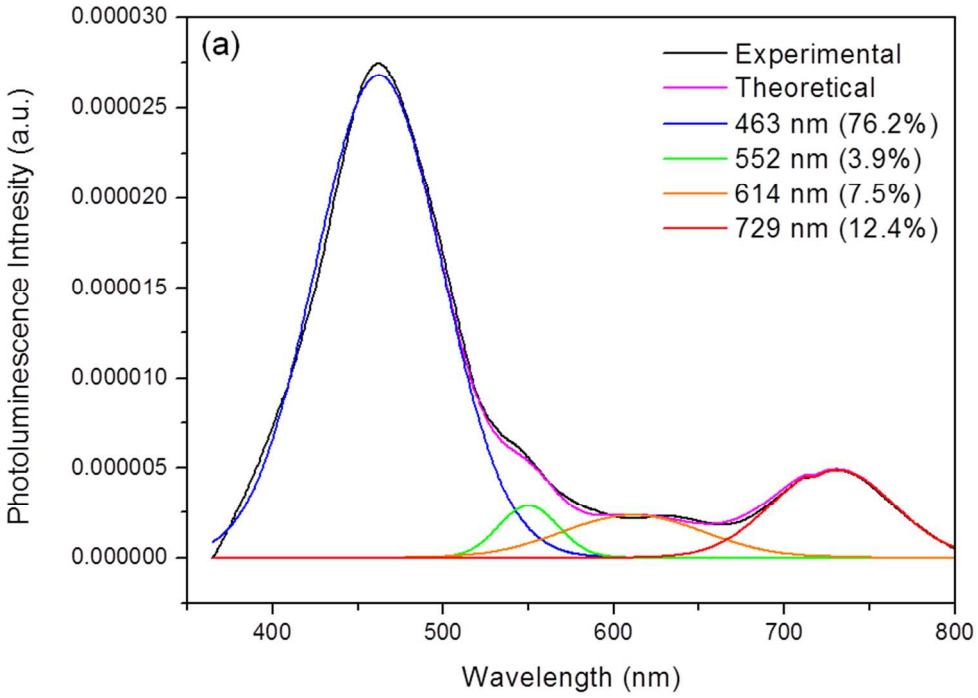

Figure 8: Photoluminescence deconvolution spectra of the Ba1-xCaxTiO3 samples: (a) x = 0; (b) x = 0.25; (c) x = 0.50; (d) x = 0.75; (e) x = 1
254x190mm (96 x 96 DPI)

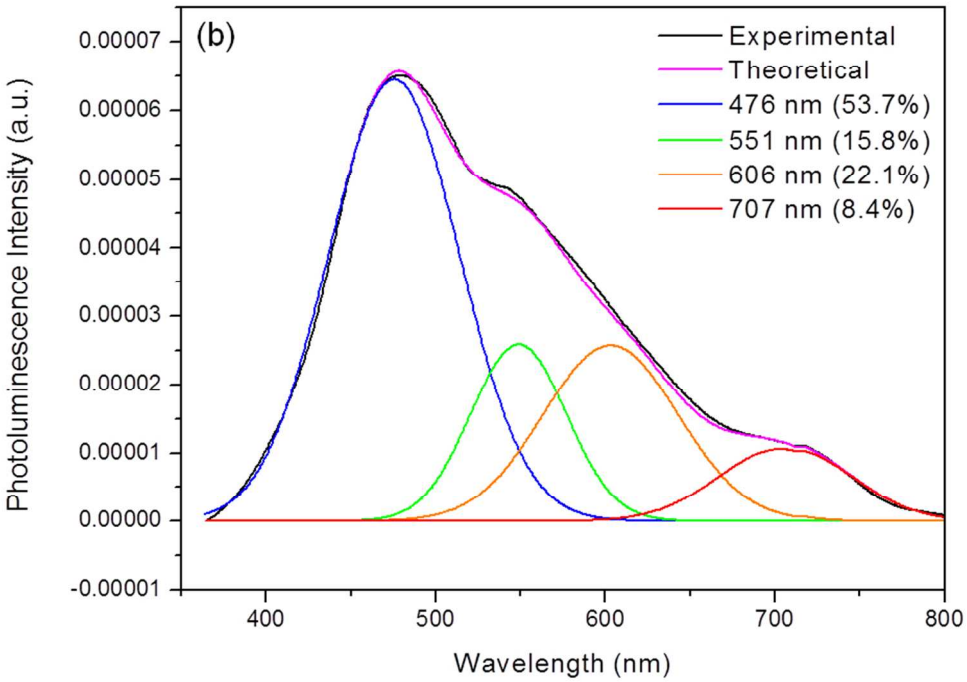

Figure 8: Photoluminescence deconvolution spectra of the Ba1-xCaxTiO3 samples: (a) x = 0; (b) x = 0.25; (c) x = 0.50; (d) x = 0.75; (e) x = 1
254x190mm (96 x 96 DPI)

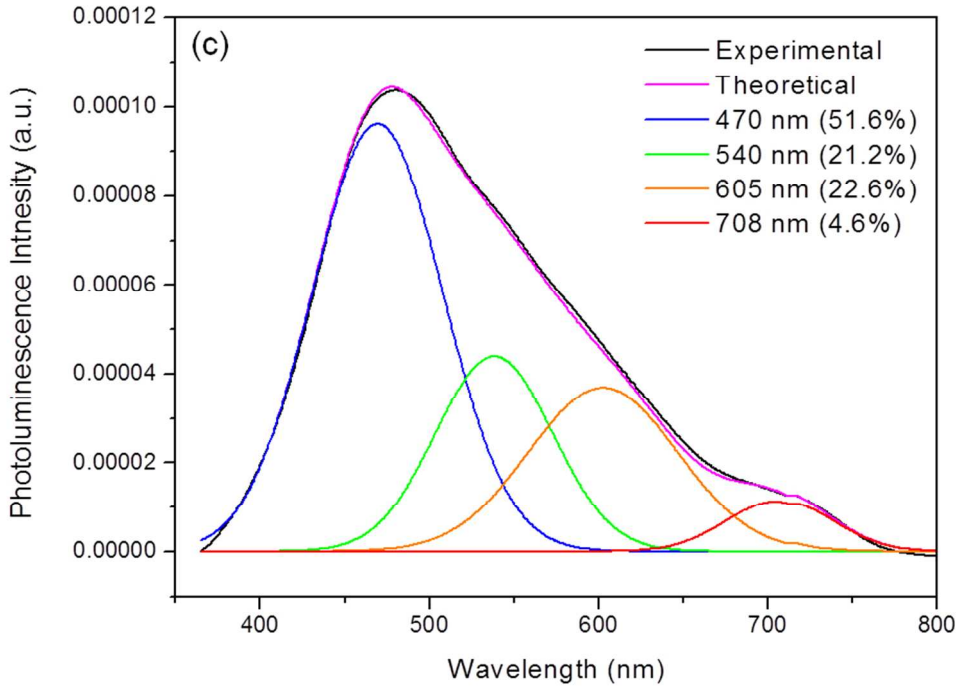

Figure 8: Photoluminescence deconvolution spectra of the Ba1-xCaxTiO3 samples: (a) x = 0; (b) x = 0.25; (c) x = 0.50; (d) x = 0.75; (e) x = 1
254x190mm (96 x 96 DPI)

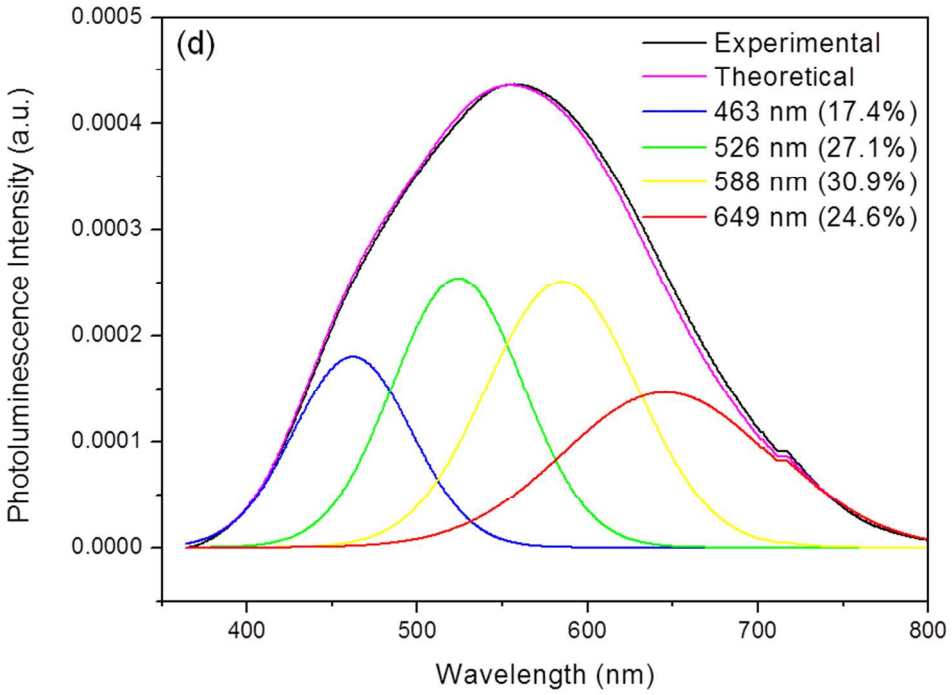

Figure 8: Photoluminescence deconvolution spectra of the Ba1-xCaxTiO3 samples: (a) x = 0; (b) x = 0.25; (c) x = 0.50; (d) x = 0.75; (e) x = 1
254x190mm (96 x 96 DPI)

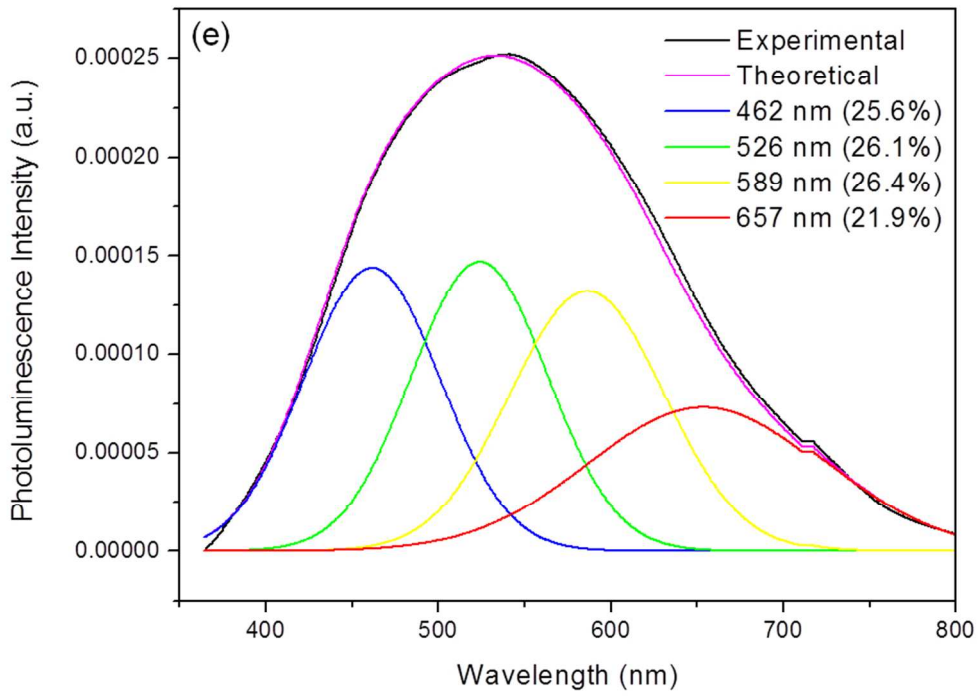

Figure 8: Photoluminescence deconvolution spectra of the Ba1-xCaxTiO3 samples: (a) x = 0; (b) x = 0.25; (c) x = 0.50; (d) x = 0.75; (e) x = 1
254x190mm (96 x 96 DPI)

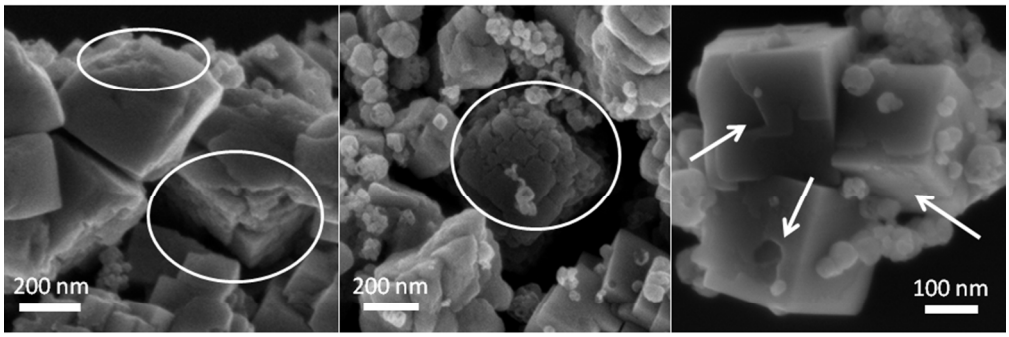

Figure 9: FE-SEM images of Ba1-xCaxTiO3 samples (x = 0.50): Particles looking like mesocrystals
254x190mm (96 x 96 DPI)

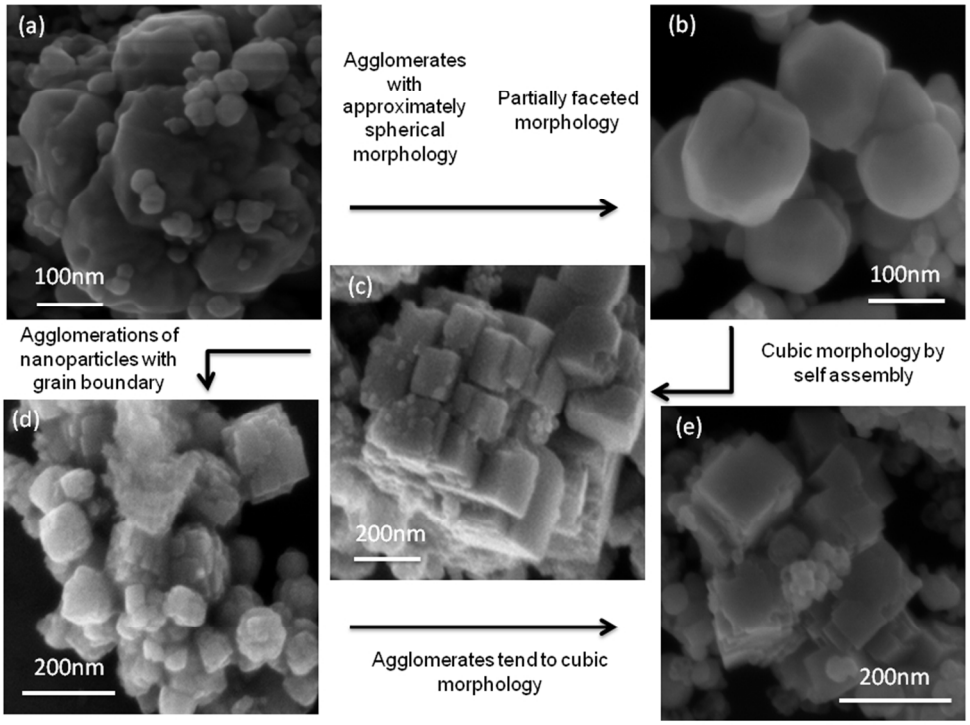

Figure 10: FE-SEM images of Ba1-xCaxTiO3 samples: (a) x = 0, (b) x = 0.25, (c) x = 0.50, (d) x = 0.75, (e) x = 1
254x190mm (96 x 96 DPI)

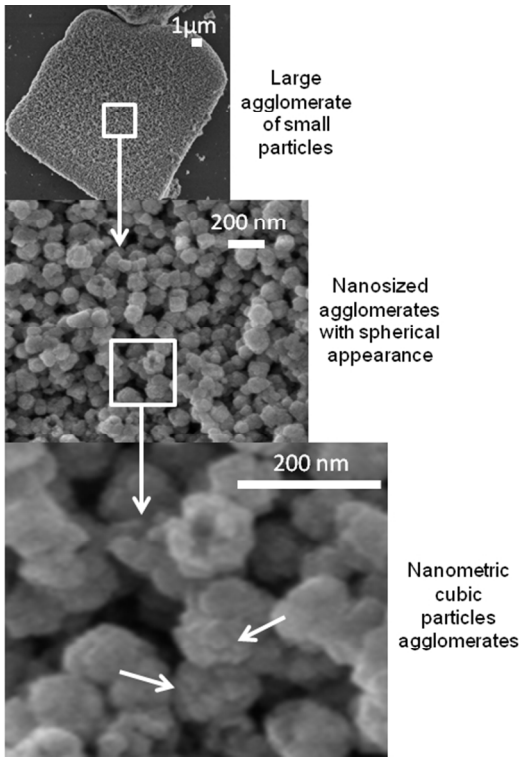

Figure 11: FE-SEM images of Ba1-xCaxTiO3 samples (x = 0.75) magnification 254x190mm (96 x 96 DPI)

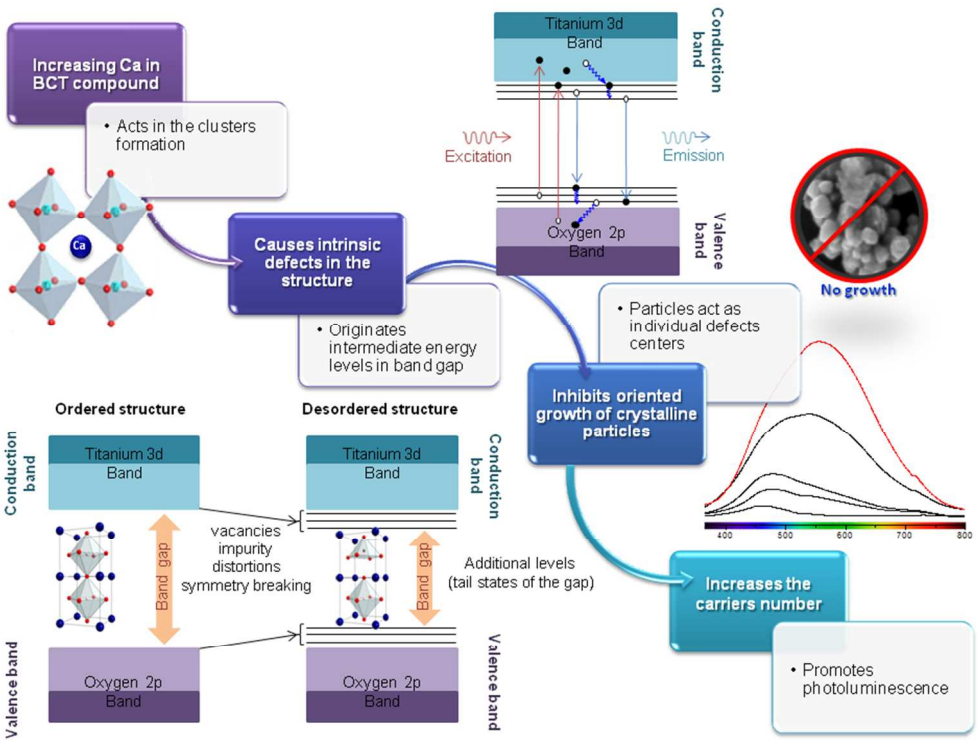

Figure 12: Schematic illustration of the defects caused by the partial substitution of lattice modifier in the compound Ba1-xCaxTiO3
254x190mm (96 x 96 DPI)